Research Square

Preprints are preliminary reports that have not undergone peer review.
They should not be considered conclusive, used to inform clinical practice,
or referenced by the media as validated information.

Digital Generating Method For Pure-Rolling Spiral Bevel Gears Based On Indexable YW-Type Milling Cutter

Rulong Tan
Chongqing University of Technology
Yang Liu
Liuxiaoba5028524570163.com

Chongqing University of Technology
Weiqing Zhang
Chongqing University of Technology
Wangwang Wang
Chongqing University of Technology
Kai Xu
Chongqing University of Technology
Feng Xiong
Chongqing University of Technology

Article

Keywords: Pure-rolling contact logarithmic spiral bevel gears, predesigned transmission error, digital generation, spatial free-form milling

Posted Date: July 27th, 2026

DOI: https://doi.org/10.21203/rs.3.rs-10401789/v1

License: This work is licensed under a Creative Commons Attribution 4.0 International License.
Read Full License

Additional Declarations: No competing interests reported.

Digital Generating Method For Pure-Rolling Spiral Bevel Gears Based On Indexable YW-Type Milling Cutter

Rulong Tan[1], Yang Liu[1*], Weiqing Zhang[1], Wangwang Wang[1], Kai Xu[1], Feng Xiong[2]
1.College of Mechanical Engineering, Chongqing University of Technology, Chongqing, 400054, China
2. School of Vehicle Engineering, Chongqing University of Technology, Chongqing, 400054, China

Abstract

To achieve high-efficiency machining and low-noise transmission, an integrated manufacturing methodology is proposed for pure-rolling contact logarithmic spiral bevel gears (PCLSBGs) that combines flank modification design with digital generating machining. Based on spatial conjugate surface theory, a parabolic transmission error (TE) function was embedded into the pinion flank modification model to ensure pure-rolling kinematic conditions during meshing. Subsequently, a digital generating machining strategy suitable for general-purpose five-axis CNC machines was developed, in which a standard YW-type tangential face mill remained fixed while rotating, and the gear blank followed a precomputed arc-shaped spatial motion trajectory, inversely derived from a modified flank geometry to generate a completely modified tooth flank through enveloping. Simulation results indicated that the machining deviation of the digitally generated flank was below 1.5 μm. Tooth contact path simulations indicated that contact points were concentrated near the middle of the tooth flank, mitigating the edge contact and stress concentration. Machining trials further confirmed that the YW mill provided a wide cutting band, thereby overcoming dense toolpaths issues associated with ball-end mills in spiral bevel gear machining.

Keywords: Pure-rolling contact logarithmic spiral bevel gears; predesigned transmission error; digital generation; spatial free-form milling;

Glossary

S_i	movable coordinate systems attached to pinion (i =1), gear (i = 2), and tool (i = c)
S_j	fixed coordinate systems corresponding to the pinion (j = 0) and gear (j = p)
Γ^i	contact path of the pinion (i = 1) or gear (i = 2)
$\Gamma^{(i)}$	modified contact path of the pinion (i = 1) or gear (i = 2)
$\boldsymbol{\Sigma}^{\boldsymbol{i}}$	tooth surface of the pinion (i = 1) or gear (i = 2)
$\Sigma^{(i)}$	modified the tooth surface of the pinion (i = 1) or gear (i = 2).
$\boldsymbol{r}_j^i$	position vector representation of Γ^i (i = 1 or 2) in the coordinate system, S_j
$\boldsymbol{r}_j^{(i)}$	position vector representation of $\Gamma^{(i)}$ (i = 1 or 2) in the coordinate system, S_j
$\boldsymbol{n}_j^i$	normalized contact direction vector representation along Γ^i (i = 1 or 2) in the coordinate system, S_j
$\boldsymbol{n}_j^{(i)}$	normalized contact direction vector of the modified tooth surface along $\Gamma^{(i)}$ (i = 1 or 2) in the coordinate system, S_j
$\boldsymbol{\alpha}^i$	tangent vector to the contact trace Γ^i of the pinion (i = 1) or gear (i = 2)
$\boldsymbol{\alpha}^{(i)}$	tangent vector to the modified contact trace $\Gamma^{(i)}$ of the pinion (i = 1) or gear (i = 2)
$\boldsymbol{v}_j^{12}$	relative velocity vector representation between pinion and gear in coordinate system S_j
φ	relative rotation angle between S_0 and S_1 (rotation angle of the gear)
ϕ	relative rotation angle between S_p and S_2 (rotation angle of the pinion)

* Corresponding author.
E-mail address:liuxiaoba502852457@163.com(L. Yang)

ξ shaft angle

$\Delta\theta$ transmission error function of cone angle variable

i_{21} constant transmission ratio between pinion and gear

1. Introduction

Based on spatial conjugate curve meshing theory, pure rolling spiral bevel gears (PCSBGs) offer compelling advantages such as compact size, high reliability, low noise, excellent stability, high gear ratios, and superior load-carrying capacity, making them particularly suitable for critical applications in aerospace, marine propulsion, and mining machinery [1, 2]. Nevertheless, two fundamental challenges hinder their high-efficiency and high-precision manufacturing in practical engineering: i) the current pure rolling contact theory for bevel gears assumes a constant transmission ratio and ideal kinematic conditions but is not sufficiently tolerant of inevitable manufacturing and assembly deviations [3, 4]; and ii) conventional ball-end milling processes suffer from low material removal rates [5, 6]. In the design of PCSBGs, machining and assembly errors induce angular velocity jumps at the junctions of the meshing cycle, which lead to significant vibrations. These errors also cause the contact points to deviate from the pitch cone generatrix, thereby inducing a rolling-sliding combined motion that exacerbates the risks of pitting and scuffing. Consequently, performance enhancement through targeted flank design is critical.

Hlebanja et al. [7] defined gear tooth geometry using a semi-parabolic function derived from rack and performed flank modification and contact simulation via specialized software; however, their approach offers limited effectiveness in vibration suppression under predesigned transmission error (PTE) conditions. Huang et al. [8] proposed two breakthrough methodologies to characterize the dynamic meshing behavior of spiral bevel gears (SBGs). Specifically, they developed a mathematical model of the contact path based on tooth trace lines, demonstrating that when projected onto the tangent plane of the base cone, the contact curve assumes the shape of a tooth trace line, such as a circle or a logarithmic spiral, thereby exhibiting contact characteristics analogous to those of cylindrical gears. Simon [9] focused on design and manufacturing methodologies aimed at reducing TE in spiral bevel gears, demonstrating that significant improvements in the accuracy and stability of the gear drive system can be achieved through refined tooth geometry and enhanced manufacturing processes. Li et al. [10] proposed a multi-objective optimization framework for spiral bevel gears, with a primary focus on enhancing contact performance and meshing efficiency. Zhang et al. [11] integrated dynamic equation analysis with dynamic stress computation to establish a similarity theory and corresponding correction methodology for gear system dynamic stresses that explicitly accounts for geometric distortions. This framework enables accurate prediction of the dynamic stress response in full-scale prototype gear systems through scaled-model experiments. Sciarra et al. [12] addressed the inherent geometric disparities across transverse sections of bevel gears and, for the first time, introduced the concept of axial contact ratio, thereby refining the evaluation framework for bevel gear meshing characteristics. Simon [13] developed a multi-objective optimization technique specifically tailored for the production of face-milled hypoid gears, enabling precise and efficient manufacturing through CNC machine tools.

In gear manufacturing, the use of specialized disk cutters for large-scale spiral bevel gears incurs high production costs and short tool life. With the advancement in freeform digital machining technologies, ball-end mills have been employed to produce large-scale spiral bevel gears. However, owing to the limited cutting width and low material removal rates inherent in ball-end milling, achieving both high efficiency and precision remains challenging [14]. Researchers have developed

advanced methods aimed at overcoming these limitations. Mu et al. [15] achieved the machining of face-milled spiral bevel gears by replacing traditional straight-flank tools with arc-flank tools. By controlling the geometric parameters of the arc-flank, localized tooth surface modifications were achieved, resulting in symmetrical TE curves after modification. Litvin et al. [16] utilized computer simulations to generate shaper cutter paths for modified gears. By applying double-crowning modifications and parabolic error functions, they achieved tooth-surface modifications, error compensation, and noise reduction. The use of parabolic edge tools facilitated efficient and precise gear machining. Liu et al. [17] established a comprehensive digital technology chain from high-precision virtual tooth surface generation to load-carrying contact analysis (LTCA). By integrating Python-driven parametric modeling, VERICUT virtual machining simulations, and semi-analytical LTCA models, they enhanced the design and manufacturing efficiency of spiral bevel gears. Wang et al. [18] applied skiving techniques to the manufacturing of internal spiral bevel gears. Based on Python-derived theoretical tooth surfaces, they imported data into VERICUT for virtual machining and validated the tool paths in real time to ensure an interference-free operation. This successfully generated complete tooth profiles for internal hypocycloidal bevel gears. Choudhary et al. [19] conducted in-depth studies on the modeling and simulation of bevel gears. They developed a novel modeling approach and validated its performance under various operating conditions through simulations. This research not only streamlined the design process, but also improved the accuracy of the design outcomes, providing new insights for future bevel gear designs. Das et al. [20] investigated strategies to reduce machining time in bevel gear production. Their high-efficiency operational methods not only shortened machining time, but also increased production efficiency.

In our previous work, fundamental conditions required for pure rolling contact in spiral bevel gears were established based on spatial conjugate curve theory, and an analytical kinematic-geometric model of PCSBGs was derived [21, 22]. However, post-machining evaluations revealed that the gear pair exhibited low tolerance to assembly variations, and the machining efficiency on using ball-end mills was insufficient. To address these challenges, this study integrates the PTE theory, digital generating machining, and YW mills into a unified manufacturing framework for pure rolling spiral bevel gears, aiming to simultaneously enhance transmission performance and machining efficiency. Specifically, the tooth flank equation of the PLSBGs was first derived analytically. Subsequently, the PTE was incorporated into the flank modification process. Cutter location points were then computed using a YW mill to enable digitally generated machining. Finally, small-batch prototypes of the PLSBGs were manufactured on a vertical five-axis CNC machine tool, followed by contact pattern analysis to evaluate the meshing performance.

2. Geometry of PLSBGs

Based on the spatial conjugate curve theory [23], this section derives the tooth flank modification equation for pure rolling logarithmic spiral bevel gears with a PTE to control the shape of the TE curve.

2.1. Applied coordinate systems

Based on the establishment of a mathematical model for pure rolling spiral bevel gear tooth surfaces using spatial conjugate curve meshing theory, an application coordinate system was established, as shown in Fig. 1. S_0 and S_p are two fixed right-handed orthogonal coordinate systems in space, and the moving coordinate systems S_1 and S_2 correspond to the pinion and gear tooth surfaces, respectively. Γ^1 and Γ^2 represent the theoretical contact paths on the pinion and gear tooth surfaces, respectively. The angle between the two rotational axes is denoted by ξ. The relative rotation angle

between S_0 and S_1 is φ, and that between S_p and S_2 is ϕ. M denotes the instantaneous contact point. According to the definition of transmission ratio, $|\omega^2| = i_{21}|\omega^1|$. Hence, ϕ can be expressed as

$$\phi = i_{21}\varphi . \tag{2}$$

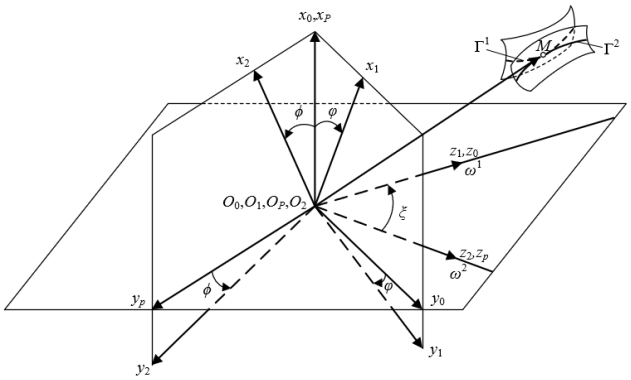


Fig. 1. Applied coordinate systems.

2.2. Spatial conjugate curves

In the spatial conjugate meshing theory, an arbitrary spatial regular curve denoted as Γ^1 can be selected as the contact path of one of the gears. Then, based on the contact direction and meshing conditions along Γ^1, its conjugate curve, denoted as Γ^2, can be derived [24].

For pure rolling contact bevel gears, the tooth trace is a conical helix, meaning that the intersection between the tooth surface and pitch cone is a conical helix (Fig. 2). During the meshing, the motion trajectory of the contact point in the rotating coordinate system of each gear must lie on its pitch cone. Selecting the conical helix Γ^1 as the contact path of the pinion, the position vector $\boldsymbol{r}^1$ of Γ^1 in the S_1 coordinate system can be expressed by a parametric equation as follows:

$$\boldsymbol{r}_1^1(t) = \begin{pmatrix} pf(t)\sin(t) & pf(t)\cos(t) & f(t) & 1 \end{pmatrix}^{\mathrm{T}}, \tag{3}$$

where $f(t)$ is an arbitrary function with C^2 continuity, $p=\tan(\delta_1)$, and δ_1 denotes the pitch cone angle of the pinion, satisfying $0<\delta_1<\pi/2$.

In Fig. 2, S_c denotes the tool coordinate system, and $\boldsymbol{\alpha}^1$ represents the tangent vector of the contact trace Γ^1.

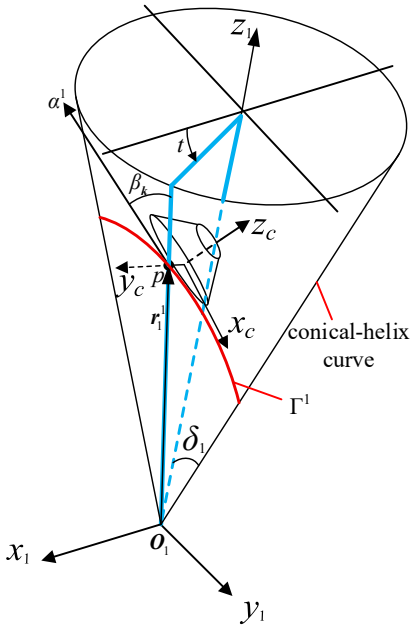


Fig. 2. Diagram of a conical helix.

Based on the gear geometry theory, the relative velocity $\boldsymbol{v}_0^{12}$ between the driving and driven gears can be derived. Through coordinate transformation, the relative motion velocity $\boldsymbol{v}_1^{12}$ in coordinate system S_1 was obtained as follows:

$$\boldsymbol{v}_1^{12} = \omega_1^1 \times \boldsymbol{r}_1^1 - \omega_1^2 \times \boldsymbol{r}_1^1 = \boldsymbol{M}_{10}\boldsymbol{v}_0^{12}. \tag{4}$$

In the tooth surface design, the gear meshing equation must hold. For any normal vector $\boldsymbol{n}^1$ of the contact path Γ^1, the following condition is satisfied:

$$\boldsymbol{n}^1 \cdot \boldsymbol{v}^{12} = 0. \tag{5}$$

2.3. Model of continuous PCLSBGs

A pure rolling contact implies that the magnitude of the relative velocity at the contact point is zero, indicating that

$$\boldsymbol{v}_1^{12} = 0. \tag{6}$$

Based on Eqs. (2) and (3), the relative velocity in the S_1 coordinate system can be derived as

$$\boldsymbol{v}_1^{12} = \begin{pmatrix} f(t)\left(p\cos t\left(i_{21}\cos\xi - 1\right) - i_{21}\sin\xi\cos\varphi\right) \\ f(t)\left(i_{21}\sin\xi\sin\varphi + \sin t\left(p - i_{21}p\cos\xi\right)\right) \\ i_{21}pf(t)\sin\xi\sin(t-\varphi) \\ 0 \end{pmatrix}. \tag{7}$$

Substituting Eq. (6) into Eq. (5) and assuming $\varphi \neq 0$, the condition for continuous pure rolling becomes

$$\begin{cases} t = \varphi \\ p = \dfrac{i_{21}\sin\xi}{-1 + i_{21}\cos\xi} \end{cases}. \tag{8}$$

In this study, taking the tooth flank of the PCLSBGs as an example, the contact path was defined as a logarithmic spiral. The corresponding parametric representation of the contact trace Γ^1 is given by

$$\begin{cases} p = \dfrac{n}{b} \\ f(t) = be^{mt} \end{cases}, \tag{9}$$

where $n=\sin(\delta_1)$, $m=\sin(\delta_1)\cot(\beta_k)$, and $b=\cos(\delta_1)$. Here, δ_1 denotes the pitch cone angle of the pinion, and β_k is the angle between the tangent vector of the logarithmic spiral and the corresponding generator of the cone. Based on the condition for continuous pure rolling contact, the calculation formula for the pitch cone angle δ_1 is given by

$$\delta_1 = \tan^{-1}\left(\frac{i_{21}\sin\xi}{-1 + i_{21}\cos\xi}\right). \tag{10}$$

Based on Eqs. (2) and (8), the specific form of the contact trace Γ^1 as a logarithmic spiral in the S_1 coordinate system is given by:

$$\boldsymbol{r}_1^1(t) = \begin{pmatrix} ne^{mt}\sin(t) & ne^{mt}\cos(t) & be^{mt} & 1 \end{pmatrix}^{\mathrm{T}}. \tag{11}$$

After determining the equation of the contact trace Γ^1, the conjugate curve Γ^2 is obtained by applying coordinate transformation under the condition of continuous pure rolling contact. In the S_2 coordinate system, the parametric equation of the contact trace Γ^2, denoted as $\boldsymbol{r}_2^2(t)$, is calculated as

$$\boldsymbol{r}_2^2(t) = M_{21}(t)r_1^1(t) = \begin{pmatrix} e^{mt}\sin(i_{21}t)(n\cos(\xi) - b\sin(\xi)) \\ e^{mt}\cos(i_{21}t)(n\cos(\xi) - b\sin(\xi)) \\ e^{mt}(b\cos(\xi) + n\sin(\xi)) \\ 1 \end{pmatrix}. \tag{12}$$

2.4. Tooth flank modification with PTE

To reduce the sensitivity to assembly errors and mitigate vibrations [25], this study proposes a tooth flank modification method based on the PTE. The pinion tooth surface is modified parabolically along the tooth length direction. By rotating each instantaneous contact point on the theoretical contact trace Γ^1 around its corresponding pitch cone generator, a modified target curve $\Gamma^{(1)}$ is generated. The

rotation angle for each point varies according to the PTE function $\Delta\theta(t)$. Consequently, the tooth trace of the pinion is redefined from the original Γ^1 to the modified target curve $\Gamma^{(1)}$, as illustrated in Fig. 3.

The angular difference between Γ^1 and $\Gamma^{(1)}$ can be regarded as the transmission error. Assuming that the modified tooth surface contact trace $\Gamma^{(1)}$ undergoes a displacement, the TE function $\Delta\theta(t)$ can be designed as

$$\Delta\theta(t) = -\kappa(t-\varepsilon)^2, \tag{13}$$

where κ is the parabolic coefficient, t is the conical angular parameter variable, and ε denotes the conical angle parameter at the design reference point.

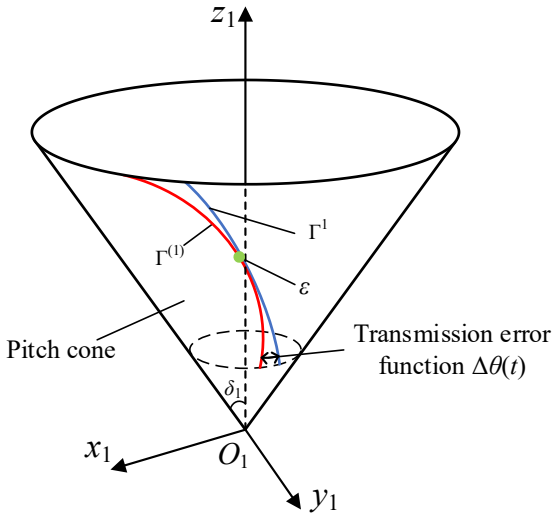


Fig. 3. Modified target curve.

Since Γ^1 and $\Gamma^{(1)}$ coincide only at the design reference point ε, the TE is 0 when the contact point is located at this position. Fig. 4 illustrates the TE curve for multitooth engagement.

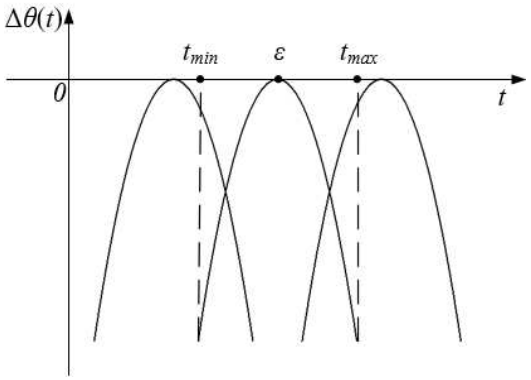


Fig. 4. PTE curve.

Under single-tooth engagement conditions, the TE amplitudes at the endpoints of the modified target curve $\Gamma^{(1)}$ can be set equal ($\Delta\theta(t_{\min})=\Delta\theta(t_{\max})$). Therefore, the design reference point ε can be selected as the midpoint of the theoretical contact trace.

Based on the relative positional relationship between the modified target curve $\Gamma^{(1)}$ and theoretical contact trace Γ^1, and substituting the TE function $\Delta\theta(t)$ into Eq.(3), the position vector equation of the modified target curve $\Gamma^{(1)}$—denoted as $\boldsymbol{r}_1^{(1)}(t)$—can be obtained as follows:

$$\boldsymbol{r}_1^{(1)}(t) = \begin{pmatrix} pf(t)\sin(t-\Delta\theta(t)) & pf(t)\cos(t-\Delta\theta(t)) & f(t) & 1 \end{pmatrix}^{\mathrm{T}}. \tag{14}$$

From Eq. (13), the unit tangent vector of the modified target curve $\Gamma^{(1)}$ can be calculated as

$$\boldsymbol{\alpha}^{(1)}(t)=\frac{\mathrm{d}\boldsymbol{r}_1^{(1)}(t)/\mathrm{d}t}{\left|\mathrm{d}\boldsymbol{r}_1^{(1)}(t)/\mathrm{d}t\right|}. \tag{15}$$

To establish a direct relationship between the unit normal vector $\boldsymbol{n}^{(1)}$ and normal pressure angle α_n,

$$\boldsymbol{n}^{(1)}(t)=\begin{pmatrix}\boldsymbol{n}_x^{(1)} & \boldsymbol{n}_y^{(1)} & \boldsymbol{n}_z^{(1)} & 0\end{pmatrix}^{\mathrm{T}}. \tag{16}$$

Here, $\boldsymbol{n}_x^{(1)},\boldsymbol{n}_y^{(1)},\boldsymbol{n}_z^{(1)}$ represent the components of the normal vector along the respective coordinate axes and are explicitly expressed as follows:

$$\begin{cases}\boldsymbol{n}_x^{(1)}=\left((C_{(\alpha)}f'(t)-p^2f'(t)f(t)\Delta t'\sin(\alpha_n))\cos(\Delta t)+C_\eta\sin(\alpha_n)\sin(\Delta t)\right)\Big/C_\beta\\ \boldsymbol{n}_y^{(1)}=\left((p^2f'(t)f(t)\Delta t'\sin(\alpha_n)-C_{(\alpha)}f'(t))\sin(\Delta t)+C_\eta\sin(\alpha_n)\cos(\Delta t)\right)\Big/C_\beta\\ \boldsymbol{n}_z^{(1)}=p\left(f'(t)^2\sin(\alpha_n)+C_{(\alpha)}f(t)\Delta t'\right)\Big/C_\beta\end{cases}, \tag{17}$$

where $\Delta t=t-\Delta\theta(t)$, and the relevant parameters are as follows:

$$\begin{cases}C_\eta=f'(t)^2+p^2f(t)^2(\Delta t')^2\\ C_{(\alpha)}=\pm\sqrt{C_\eta\cos^2(\alpha_n)-p^2f'(t)^2\sin^2(\alpha_n)}\\ C_\beta=\sqrt{C_\eta\left(C_\eta\sin^2(\alpha_n)+C_{(\alpha)}{}^2+p^2f'(t)^2\sin^2(\alpha_n)\right)}\end{cases}. \tag{18}$$

In the above equation, the positive and negative values of $C_{(\alpha)}$ correspond to the tooth surface normal vectors of the convex and concave surfaces of the pinion after modification, respectively.

The theoretical tooth surface of the pinion Σ^1 is generated by continuously varying the orthogonal cross-sectional curve $\Gamma^{(s1)}$ in the normal plane at each discrete point along the theoretical contact trace Γ^1. After redefining Γ^1, the target tooth surface of the pinion can be considered as being formed by continuously varying the cross-sectional curve $\Gamma^{s(1)}$ in the normal plane along the modified target curve $\Gamma^{(1)}$, as shown in Fig. 5. Based on this principle, a local coordinate system S_{F1} is constructed using three basis vectors at any instantaneous contact point M on the modified target curve $\Gamma^{(1)}$: $\boldsymbol{\alpha}^{(1)}$, $\boldsymbol{n}^{(1)}\times\boldsymbol{\alpha}^{(1)}$, and $\boldsymbol{n}^{(1)}$. In the coordinate system S_{F1}, the plane spanned by the basis vectors $\boldsymbol{n}^{(1)}\times\boldsymbol{\alpha}^{(1)}$ and $\boldsymbol{n}^{(1)}$ is referred to as the normal plane of the modified target curve $\Gamma^{(1)}$ at that point, as illustrated in Fig. 6.

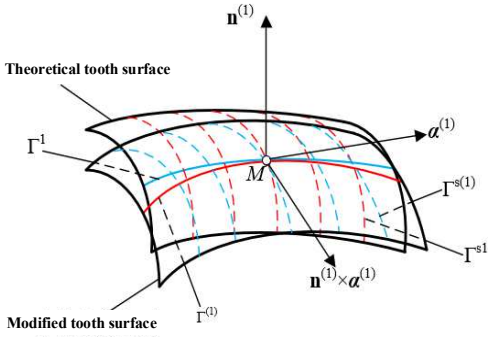


Fig. 5. Modified tooth surface of the pinion.

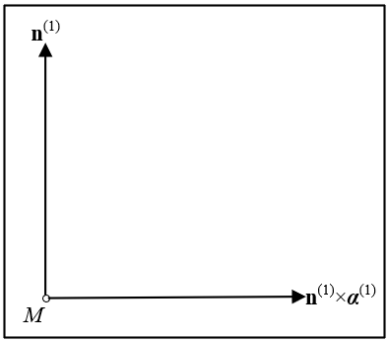


Fig. 6. Normal plane of $\Gamma^{(1)}$ at point M.

To simplify the model construction, circular arcs were selected as the cross-sectional curves for both the pinion and gear. The explicit expressions for the cross-sectional curves of the pinion and gear are as follows:

$$\begin{cases}\boldsymbol{r}_{Fr1}^{\mathrm{sec}1}(u)=(0 \quad R_1\sin(u) \quad -R_1+R_1\cos(u) \quad 1)^{\mathrm{T}}\\ \boldsymbol{r}_{Fr2}^{\mathrm{sec}2}(v)=(0 \quad -R_2\sin(v) \quad R_2-R_2\cos(v) \quad 1)^{\mathrm{T}}\end{cases}. \tag{19}$$

In the above equation, R_1 denotes the curvature radius of the pinion cross-sectional curve, and R_2 denotes the curvature radius of the gear cross-sectional curve.

For the modified gears, circular arcs were still adopted as cross-sectional curves for both the pinion and gear. According to tooth surface generation theory and after coordinate transformation, the equation of the modified pinion tooth surface $\Sigma^{(1)}$ is given as follows:

$$\boldsymbol{S}_{C1}(t,u)=\boldsymbol{M}_{1F1}(t)\boldsymbol{r}_{F1}^{\mathrm{Sec1}}(u). \tag{20}$$

Here, $M_{1F1}(t)$ represents the coordinate transformation matrix from local coordinate system S_{F1} to global coordinate system S_1. Its explicit form is as follows:

$$\boldsymbol{M}_{1F1}(t)=\begin{bmatrix} \boldsymbol{i}^{s1}\bullet\boldsymbol{\alpha}^{(1)} & (\boldsymbol{i}^{s1},\mathbf{n}^{(1)},\boldsymbol{\alpha}^{(1)}) & \boldsymbol{i}^{s1}\square\boldsymbol{\alpha}^{(1)} & \\ \boldsymbol{j}^{s1}\bullet\boldsymbol{\alpha}^{(1)} & (\boldsymbol{j}^{s1},\mathbf{n}^{(1)},\boldsymbol{\alpha}^{(1)}) & \boldsymbol{j}^{s1}\square\boldsymbol{\alpha}^{(1)} & \boldsymbol{r}_1^{(1)}(t) \\ \boldsymbol{k}^{s1}\bullet\boldsymbol{\alpha}^{(1)} & (\boldsymbol{k}^{s1},\mathbf{n}^{(1)},\boldsymbol{\alpha}^{(1)}) & \boldsymbol{k}^{s1}\square\boldsymbol{\alpha}^{(1)} & \\ 0 & 0 & 0 & \end{bmatrix}. \tag{21}$$

Considering the logarithmic spiral as the tooth trace, the logarithmic spiral located on the pitch cone is redefined as the modified target curve $^{(1)}$. In coordinate system S_1, the vector equation of $\Gamma^{(1)}$ can be expressed as

$$\boldsymbol{r}_1^{(1)}(t)=\begin{pmatrix} ne^{mt}\sin(\Delta t) & ne^{mt}\cos(\Delta t) & be^{mt} & 1 \end{pmatrix}^{\mathrm{T}}. \tag{22}$$

The design reference point ε is taken as the midpoint of the theoretical contact trace.

$$\varepsilon=\frac{t_{\min}+t_{\max}}{2}. \tag{23}$$

The TE along the tooth length direction of the pinion was calculated according to ISO 1328-1-2013 [26]. As shown in Fig. 6, the intermediate value of the TE at $t=t_{\min}$ or $t=t_{\max}$ is denoted as θ_{arcsec}, which is then converted into radians as θ_{rad}.

$$\theta_{rad}=\Delta\theta(t_{\min})=\Delta\theta(t_{\max}) \tag{24}$$

Taking $t=t_{\min}$, the parabolic coefficient κ can be calculated using Eq. (12) as follows:

$$\kappa=\frac{\theta_{rad}}{(t_{\min}-\varepsilon)^2} \tag{25}$$

$$t_{\min}=\frac{1}{m_t}\ln\left(\frac{d_{e1}-2B\sin(\delta_1)}{2n}\right) \tag{26}$$

Here, d_{e1} is the outer pitch cone diameter of the pinion, m_t is the face width modulus, and B is the tooth width.

The PTE $\Delta\theta(t)$ can be specifically expressed as

$$\Delta\theta(t)=-\frac{\theta_{rad}}{(t_{\min}-\varepsilon)^2}(t-\varepsilon)^2. \tag{27}$$

3. Digital Generating Tool Path Calculation Method

Considering the advantages of flat-end mills, such as a wide cutting width and high machining efficiency, a digital generation machining method for spiral bevel gears using a YW mill was proposed. The lead angles for the left and right tooth flanks were determined separately based on a freeform surface machining strategy using a flat-end mill, whereas the bottom of the tooth slot was defined by the tool tip position. This approach ensured a large cutting width and high machining accuracy, effectively addressing the issues associated with ball-end mills in machining centers, such as dense tool paths and compromised surface quality when processing spiral bevel gears.

3.1 Mathematical model of the YW mill

In the tool coordinate system S_c—where the origin O_c coincides with the center of the bottom face of the disk cutter—the z_c-axis aligns with the tool axis, and the y_c-axis lies on the bottom face of the disk cutter. The x_c-axis was determined using the right-hand rule. Here, O_r denotes the center of the cutting edge circle, r is the radius of the cutting edge circle, and ϕ_a represents the distance from the origin of the tool coordinate system to the tip point of the cutter (Fig. 7).

Based on the geometric characteristics of the YW mill, the position vectors of any point P_1, P_2, and P_3 on its side cutting edge, bottom cutting edge, and tip fillet, respectively, are denoted as r_{p1}, r_{p2}, and r_{p3} respectively, which can be expressed as

$$\boldsymbol{r}_{p_1}=\begin{pmatrix} 0 & \phi_a-r_c-l_{1r}\cdot\cos(\alpha_t)+r_c\cdot\sin(\alpha_t) & r_c+l_{1r}\cdot\sin(\alpha_t)+r_c\cdot\cos(\alpha_t) & 1 \end{pmatrix}^T, \tag{28}$$

$$\boldsymbol{r}_{p_2}=\begin{pmatrix} 0 & \phi_a-r_c-l_{2r} & 0 & 1 \end{pmatrix}^T, \tag{29}$$

$$\boldsymbol{r}_{p_3}=\begin{pmatrix} 0 & \phi_a-r_c+r_c\cdot\cos(\theta_r) & r_c-r_c\cdot\sin(\theta_r) & 1 \end{pmatrix}^T. \tag{30}$$

Here, $\boldsymbol{\alpha}_t$ denotes the tool tilt angle, and r_c is the radius of the cutting-edge fillet at the tool tip. The distance from an arbitrary cutting point on the side cutting edge to the tangent point between the fillet and straight-side edge is denoted as l_{1r}. Similarly, the distance from an arbitrary cutting point on the bottom cutting edge to the tangent point between the fillet and straight bottom edge is denoted by l_{2r}. The angle θ_r represents the angle between the point O_r and the positive direction of the y_c-axis. The ranges of l_{1r}, l_{2r}, and θ_r are defined as $0 \le l_{1r}$, $l_{2r} \le l_r$, and $0 \le \theta_r \le \pi/2$, respectively.

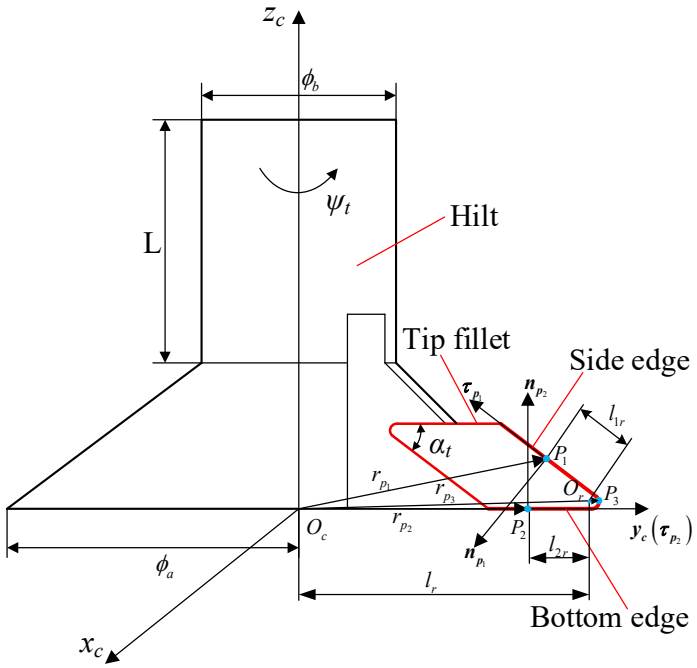


Fig. 7. Schematic diagram of the cross-section of the YW mill.

3.2 Cutter location point calculation

A YW mill often employs a variable contour milling strategy when machining tooth slots, as shown in Fig. 11. Taking the machining of the first and second layers as examples, the specific steps are as follows: i) After determining the cutting thickness, the tool moves from one end of the tooth length to the other end tangentially, thereby defining the tooth profile Ⅰ. ii) The tool performs reciprocating passes along the tooth width direction until the tooth profile Ⅱ is fully machined. iii) Then, the tool begins cutting the second layer along the tooth depth direction. It moves from one end of the tooth length to the other end tangentially to define the tooth profile Ⅱ for this layer. iv) Finally, the tool again performs reciprocating passes along the tooth width direction until the tooth profile Ⅰ for this layer is fully machined. This cycle is repeated until the entire tooth slot is completely machined.

To realize the digital generation machining process, it is necessary to analyze the relative motion between the cutting tool and workpiece gear. By establishing a gear coordinate system $\mathbf{S}_g$ for analysis, the generated motion in face milling can be regarded as an engagement process between the tool profile and gear tooth surface. Consequently, when the cutting edge of the tool machines along the contact trace, two conditions must be satisfied: i) the cutting point on the tool must coincide with the corresponding point on the contact trace; and ii) the tool profile and gear tooth surface must be tangent to each other at that point. The geometric relationship of this generating motion between the tool and workpiece gear is illustrated in Fig. 8.

Taking tooth profile I as an example, the equality condition satisfying the cutting requirement can be expressed as follows:

$$\begin{cases} \boldsymbol{\tau}_P = \boldsymbol{\tau}_{P_1} \cdot \boldsymbol{M}_{O_g O_t} \\ \boldsymbol{n}_P = \boldsymbol{n}_{P_1} \cdot \boldsymbol{M}_{O_g O_t} \end{cases}. \tag{31}$$

Here, $\boldsymbol{\tau}_p$ denotes the tangent vector of the cross-sectional curve at the contact point P, and $\boldsymbol{n}_p$ is the normal vector of the tooth surface at this point. By solving the modified tooth surface equation, the radius vector at any arbitrary point can be obtained. Therefore, the tangent vector $\boldsymbol{\tau}_p$ and normal vector $\boldsymbol{n}_p$ at any point can be expressed as follows:

$$\boldsymbol{n}_p = \boldsymbol{M}_{1F1} \cdot (0 \quad \sin(u) \quad \cos(u) \quad 0)^{\mathrm{T}}. \tag{32}$$

$$\boldsymbol{\tau}_p = \boldsymbol{n}_p \times \boldsymbol{\alpha}^{(1)}. \tag{33}$$

The radius vector of an arbitrary point on the tooth surface can be expressed as

$$\boldsymbol{r}_p = \boldsymbol{M}_{O_g O_c} \cdot \boldsymbol{r}_{p1}. \tag{34}$$

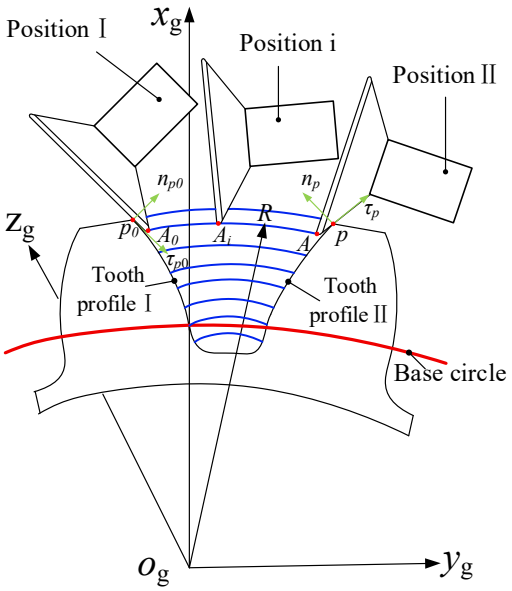


Fig. 8. Generating machining motion of the YW mill.

As shown in Fig. 7, during the machining process, the tool rapidly rotates about its main z_c-axis. To satisfy the cutting condition at all times, the tangent vector $\boldsymbol{\tau}_{p_1}$ at the cutting point P_1 must coincide with the tangent vector of the cross-sectional curve at that point, and the normal vector $\boldsymbol{n}_{p_1}$ must be collinear and opposite in direction to the normal vector of the tooth surface at that point, as illustrated in Fig. 8. In the tool coordinate system, the tangent vector $\boldsymbol{\tau}_{p_1}$ and normal vector $\boldsymbol{n}_{p_1}$ can be expressed as follows:

$$\boldsymbol{\tau}_{p_1} = (0 \quad \cos(\alpha_t) \quad -\sin(\alpha_t) \quad 0)^{\mathrm{T}}. \tag{35}$$

$$\boldsymbol{n}_{p_1} = (0 \quad -\sin(\alpha_t) \quad -\cos(\alpha_t) \quad 0)^{\mathrm{T}}. \tag{36}$$

From the mathematical model of the YW mill, $\boldsymbol{M}_{O_g O_c}$ represents a homogeneous coordinate transformation matrix from the tool coordinate system S_c to the gear coordinate system S_g. This matrix corresponds to different relative positions during the cutting process of the face mill and ensures that the tool maintains the correct contact relationship with the tooth surface throughout the machining process. The specific form is as follows:

$$\boldsymbol{M}_{O_g O_c} = (\alpha \quad \beta \quad \gamma \quad \boldsymbol{r}_{O_g O_c}). \tag{37}$$

In the above equation, $\boldsymbol{r}_{O_g O_c}$ is the radius vector from the origin O_c of the tool coordinate system S_c to the origin O_g of the gear coordinate system S_g, i.e., the tool center vector. The column vectors α, β and γ represent the homogeneous coordinate expressions of the basis vectors x_c, y_c, and z_c of the tool coordinate system S_c in the gear coordinate system S_g. These are expressed as follows:

$$\begin{cases} \alpha = (\alpha_x \quad \alpha_y \quad \alpha_z \quad 0)^{\mathrm{T}} \\ \beta = (\beta_x \quad \beta_y \quad \beta_z \quad 0)^{\mathrm{T}} \\ \gamma = \alpha \times \beta \end{cases}. \tag{38}$$

The tool center vector $\boldsymbol{r}_{O_gO_c}$ can be expressed in the gear coordinate system S_g as

$$\boldsymbol{r}_{O_gO_c} = (d_x \quad d_y \quad d_z \quad 1)^{\mathrm{T}}. \tag{39}$$

To solve for the corresponding tool-center coordinates and tool-axis vector, the procedure is described as follows. Eqs. (30) and (33) are independent. By solving them simultaneously, a coordinate transformation matrix can be obtained, from which the tool-center coordinates can be further derived. After obtaining the coordinate transformation matrix $\boldsymbol{M}_{O_gO_c}$, the vector γ represents the expression of the basis vector z_c of the tool coordinate system S_c in the gear coordinate system S_g, thereby yielding the tool axis vector. The tool center coordinates and tool axis vector together constitute the cutter location point. The same method can be applied to the calculation of cutter location points in large-gear machining.

When the parameter angle u of the cross-sectional curve is fixed, a specific instantaneous contact trajectory can be generated by varying the conical angular variable t. By substituting the relevant parameters of the tooth surface points along this trajectory into the above calculations, the corresponding machining cutter location points can be determined. These cutter location points are used as boundary conditions for the tool path. By performing an intermediate interpolation, a complete machining tool path for the entire tooth slot can be generated.

To prevent geometric interference between the tool profile and tooth surface boundary during intermediate tool path machining, the following constraint conditions must be satisfied: tool tip point P_3 must coincide with points A and A_0, and their position and normal vectors in the gear coordinate system S_g must be equal. When the cutting position is at point P or P_0, the actual cutting depth in the tooth height direction is determined by the vertex of the tool-tip fillet P_3. Under this condition, points A and A_0 must lie on the same conical surface to avoid geometric interference between the tool profile and tooth surface boundary during intermediate tool path machining. The mathematical expression for this condition can be formulated as

$$\boldsymbol{r}_{A,A_0} = \left(R\sin(t) \quad R\cos(t) \quad R/\tan(\delta) \quad 1\right)^{\mathrm{T}}. \tag{40}$$

Here, R denotes the radius of the conical surface, and δ represents the cone angle of the conical surface.

When the dovetail milling cutter is in position I, the following condition must be satisfied:

$$\boldsymbol{r}_{A_0} = \boldsymbol{M}_{O_gO_c}(\mathrm{I}) \cdot \boldsymbol{r}_{P_3}. \tag{41}$$

By solving Eqs. (39) and (40), the conical surface radius corresponding to point P_3 of the tool at position I can be obtained as follows: When the tool moves along the instantaneous contact trace, the conical angle t varies, resulting in different conical radii. When the dovetail milling cutter is in position II, to ensure consistent cutting depth for this layer, points A and A_0 must lie on a cone with the same radius. Therefore, the origin of the tool coordinate system at position II should be translated along the tangent vector $\boldsymbol{\tau}_p$ by a factor of k, leading to

$$\boldsymbol{r}_A = \boldsymbol{M}_{O_gO_c}(\mathrm{II}) \cdot \boldsymbol{r}_{P_3} + k \cdot \boldsymbol{\tau}_p. \tag{42}$$

After substituting the relevant parameters obtained from position I into Eq. (39), Eq. (39) and (41) are solved simultaneously to determine the parameter k. Based on this, the tool center coordinates and tool axis vector at position II under the same cutting depth can be obtained.

After determining the tooth slot width based on the blank design parameters, equally spaced interpolation is performed between points A and A_0 to obtain the intermediate points A_i and position

vectors r_{A_i} of the intermediate tooth slot cutting points. Using Eq. (42), the relative pose matrix $\boldsymbol{M}_{O_g O_c}(i)$ at position i is solved by the aforementioned method, yielding the tool center vector $\boldsymbol{r}_{O_g O_c}(i)$ and tool axis vector $\gamma(i)$ for the intermediate reciprocating tool path.

$$\boldsymbol{r}_{A_i} = \boldsymbol{M}_{O_g O_c}(i) \cdot \boldsymbol{r}_{P_3} . \tag{42}$$

The instantaneous contact trajectory corresponding to the boundary of the next tooth surface layer was obtained by changing the parameter angle u. The tool then followed this contact trajectory, progressively cutting inward from the outermost layer. Thus, the entire tooth-slot machining process was completed.

4. Sample Case

Based on the derivation above, the tooth surfaces of a pair of PCLSBGs with PTE were obtained. The geometric parameters of the pinion and gear were set as listed in Table 1, and a modified three-dimensional solid model of the PCLSBGs was generated accordingly, as shown in Fig. 9.

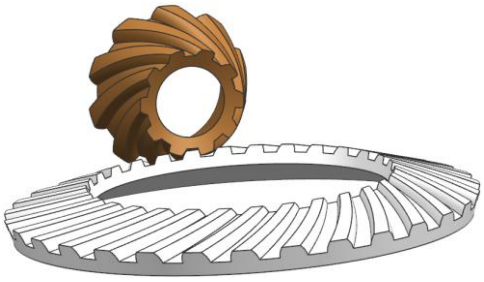


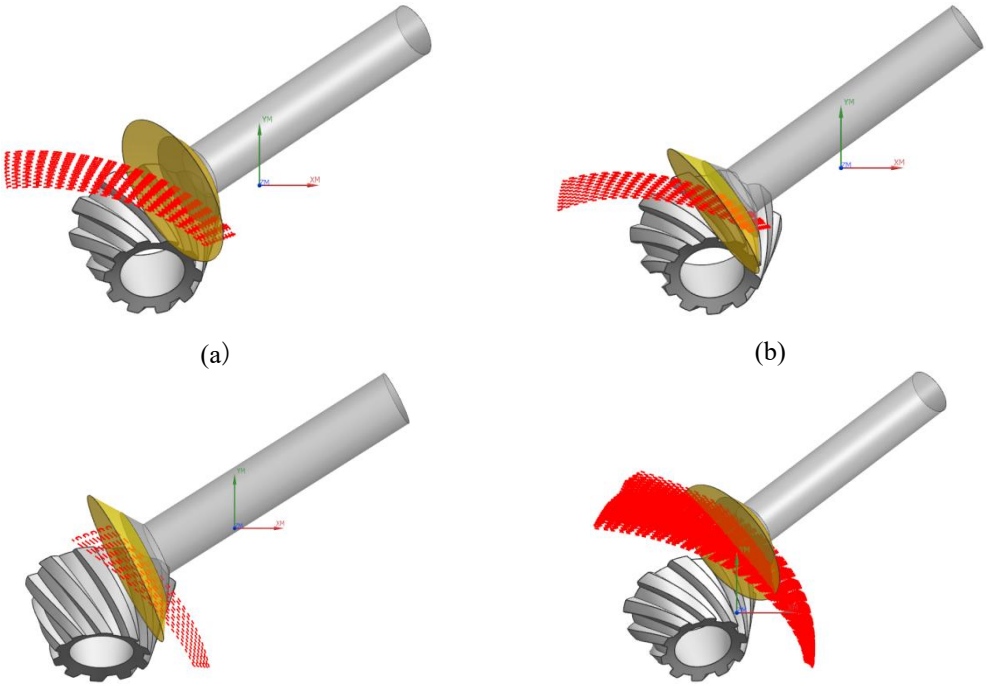
Fig. 9. Modified PCLSBG model.

Table 1 Gear design parameters

Items	Symbol	Value
Module at large end	m_t /mm	7
Pressure angle	α_n / (°)	20
Helix angle	β_k / (°)	35
Bottom clearance coefficient	C^*	0.15
Tooth height coefficient	h_c	0.3
Pitch cone angle	δ_1, δ_2 / (°)	18.435 , 71.565
Addendum angle	θ_a / (°)	1.087
Dedendum angle	θ_f / (°)	1.630
Face cone angle	δ_{a1}, δ_{a2} / (°)	19.522 , 72.652
Root cone angle	δ_{f1}, δ_{f2} / (°)	16.805 , 69.935
Tooth number	z_1 , z_2	10 , 30
Shaft angle	ξ / (°)	90
Outer pitch cone diameter	d_{e1}, d_{e2} /mm	54 , 162
Face width	β /mm	30

4.1 Machining accuracy assessment of the digitally generated flank

By inputting the gear parameters into the cutter location calculation model, a complete set of cutter location points for the entire tooth slot was obtained, as shown in Fig. 10. In digital generation machining, the cutting process is realized by controlling the variations in the tool center coordinates and tool axis vector, thereby adjusting the position and orientation of the cutter. The cutting point of the tool is defined as the tracking point. The machining error of the digital generation method can be evaluated by analyzing the distance between this tracking point and the machined tooth surface during the cutting process.

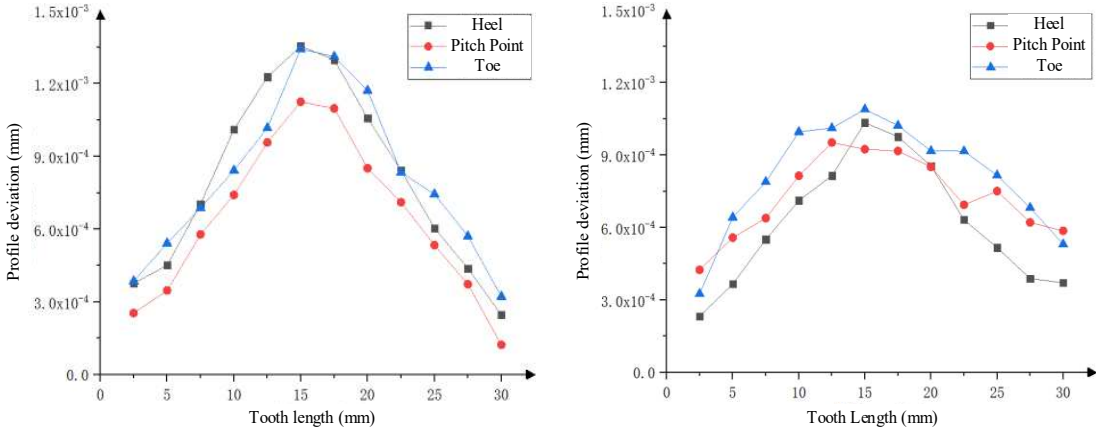


(a) (b)

(c) (d)

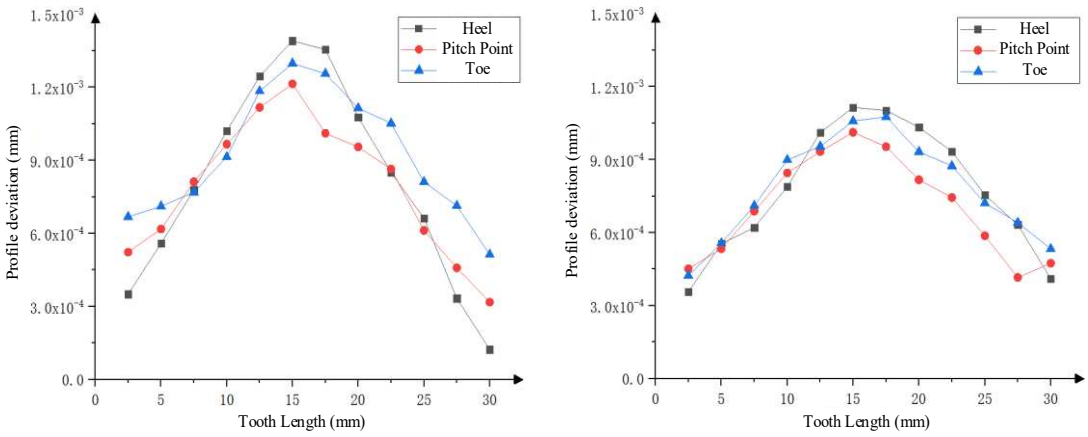
Fig. 10. Cutter location points for machining: (a) Concave surface boundary, (b) convex surface boundary, (c) single-layer reciprocating cutting, and (d) complete tooth slot.

Figs. 11 and 12 present the machining error profiles of a modified pinion tooth surface generated using a dovetail milling cutter. Twelve equally spaced points were selected along the tooth length direction within a range of 0—30 mm, and the machining error was evaluated by measuring the distances between the tracking point and three characteristic regions of the machined tooth surface—the addendum, pitch line, and dedendum.



(a) (b)

Fig. 11. Profile deviation along tooth length direction after pinion machining: (a) Concave surface and (b) Convex surface.



(a) (b)

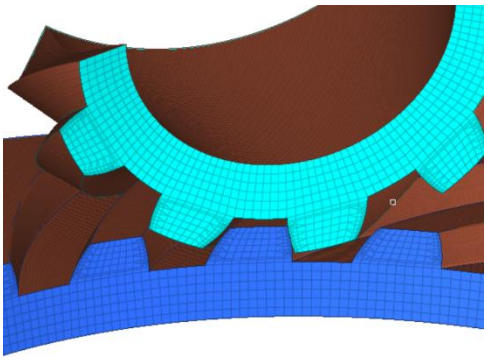
Fig. 12. Profile deviation along tooth length direction after gear machining: (a) Concave surface and (b) Convex surface.

For both the concave and convex sides, the machining error first increased and then decreased with increasing tooth length, with the maximum error occurring near the middle of the tooth surface. Moreover, the convex side exhibited lower machining errors than the concave side.

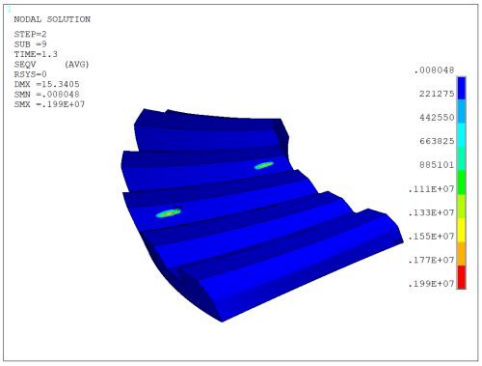
Overall, the total error band across the entire tooth surface of both the pinion and gear was within 0.0015 mm (1.5 μm). This level of accuracy has a negligible impact on the meshing performance of the bevel gear pair, thereby validating the feasibility of the proposed digital generation machining method. Furthermore, both the pinion and gear can be machined using the same dovetail milling cutter, which not only enhances the process controllability but also improves the manufacturing economy.

4.2 Numerical simulation of contact paths

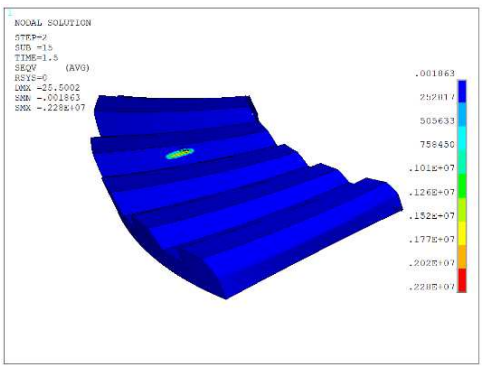
This section presents a tooth contact analysis of PLSBGs conducted via finite element analysis (FEA). The mechanical behaviors of the PLSBGs were evaluated based on this analysis, as illustrated in Fig. 13(a).



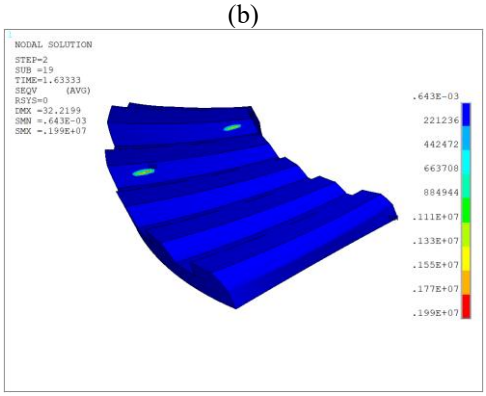
(a)



(b)



(c)



(d)

Fig. 13. Contact analysis under load for modified gear: (a) meshing pattern, (b) first actual meshing transition point, (c) contact point at mid-tooth region, and (d) second actual meshing transition point.

A five-tooth-pair finite-element model was constructed. In this model, the contacting tooth surfaces were discretized using low-order hexahedral elements with a characteristic element size of 0.2 mm, whereas the remaining regions employed a coarser mesh with a characteristic size of 2 mm. An augmented Lagrangian method was adopted as the contact algorithm to compute the pressure transmission across the interfaces. The loading system was formulated based on the energy equivalence principle, transforming the three-dimensional contact problem into a quasistatic solution framework. The boundary conditions are presented in Table 2.

The stress distributions of the PLSBGs under load after completion of the solver calculations are shown in Figs. 13(b–d). In Fig. 13(b), the actual meshing transition point 1 indicates the moment at which the previous tooth begins to disengage, and the next tooth begins to engage. As the contact point moved from the engagement start position toward the middle of the tooth surface, only a single tooth pair remained in contact (Fig. 13(c)). Finally, Fig. 13(d) shows the actual meshing transition point 2, marking the transition where the current tooth begins to disengage, and the subsequent tooth starts to enter the mesh.

Table 2 Boundary conditions

Young's modulus	Poisson's ratio	Input		Output
205 GPa	0.3	+150 N·m	+0.3 rad/s	-500 N·m

Based on the FEA results, the TE curve was derived and compared with the preset theoretical TE curve. The results of the comparative analysis are shown in Fig. 14. The blue dotted line represents the actual TE curve derived via FEA, and the red solid line represents the preset theoretical TE curve, which is drawn based on the TE function calculated according to Eq. (26). Comparison shows only a slight deviation between the actual and preset theoretical TE curves.

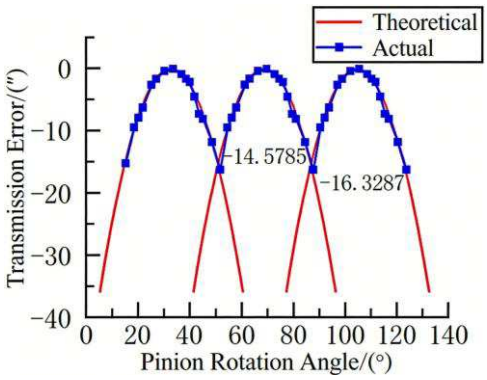


Fig. 14. Comparison of FEA and theoretical TE curves.

In the case of the multi-tooth pair meshing transmission, the intersection points of the TE curves correspond to the actual meshing transition points during the gear meshing process. At these points, the amplitude of the actual TE curve is -16.3287, while that of the theoretical TE curve is -14.5785. Although the deviation at the meshing transition points is slightly larger than that at the other contact points, the two curves coincide. Furthermore, the actual TE curve shows a parabolic shape, which is beneficial for reducing the error sensitivity and minimizing vibration and noise. This confirms the effectiveness of tooth surface modification.

Corresponding to these results, Fig. 15. shows the projection of the tooth surface contact trace onto the axial section plane, where the left and right endpoints of the contact trace are the actual engagement point T_a and actual disengagement point T_b of the gear meshing, respectively.

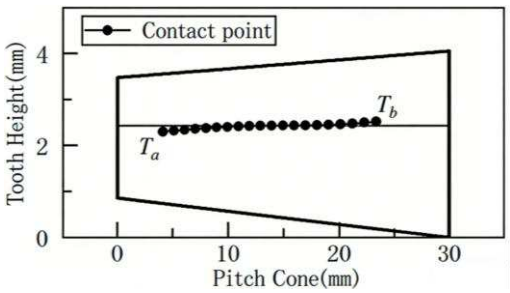


Fig. 15. Tooth surface contact trace.

The coordinates of the actual engagement point T_a and actual disengagement point T_b are (4.144, 2.299) and (23.296, 2.5106), respectively. Clearly, the actual engagement point is significantly away from the small end and biased toward the root side of the tooth, and the actual disengagement point is also far from the large end and biased toward the tip side. Consequently, the overall contact zone is centered toward the middle of the tooth surface, which helps avoid edge contact and stress concentration.

4.3 Machining experiment

Both the gear and pinion machining experiments were performed using the YW mill arbor, which can accommodate three inserts, as shown in Fig. 16. The cutter parameters are listed in Table 3.



Fig. 16. YW mill.

Table 3 Geometric parameters of the YW mill

Items	Symbol	Value
Cutter tip radius	ϕ_a/mm	30
Cutter inclination angle	α_t / (°)	35
Cutter tip fillet radius	r_c/*mm*	0.4
Cutter shank length	L	100
Cutter shank diameter	ϕ_b/mm	20
Insert mounting hole Diameter	ϕ_c/mm	4.4
Cutter length	*l*/*mm*	14.6

The verified CNC program code was imported into a general-purpose five-axis machine tool to perform actual machining on two gear blanks made of 45 steel. Subsequently, the machined PCLSBGs (modified bevel gears) were subjected to rolling tests using a spiral bevel gear integrated rolling test machine to observe the resulting contact patterns, as shown in Figs. 17. Red lead powder was applied to both the pinion and the main working tooth surfaces of the gear. After the rolling test, the meshing marks between the tooth surfaces were located near the pitch line, with the overall contact area situated in the middle of the tooth surface. The actual contact patterns closely matched the results of the modified tooth surface contact analysis, thus meeting the design requirements of PCLSBGs.

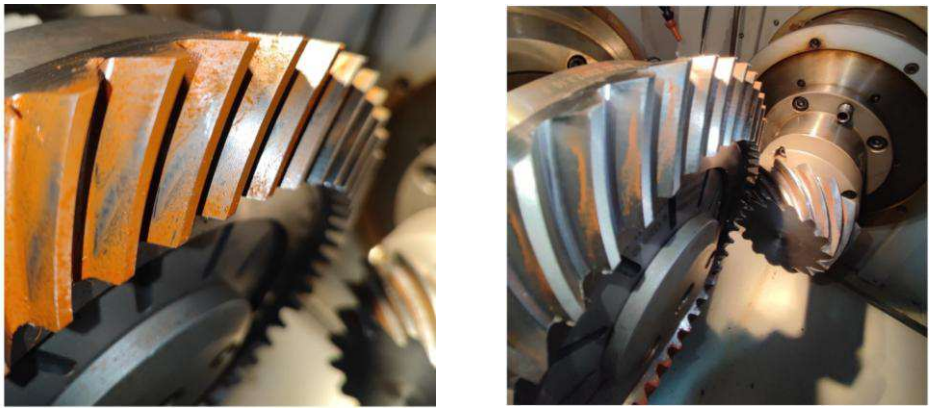


Fig. 17. Contact pattern after rolling test.

5. Conclusions

Based on the gear theory and spatial conjugate surface theory, a tooth flank modification method with a predesigned transmission error was developed and integrated into a digital generating machining framework for spiral bevel gears. A pair of pure-rolling contact logarithmic spiral bevel gears was manufactured using a standard YW-type tangential face mill and subsequently validated through rolling inspection. The following conclusions were drawn from this study.

1. A flank modification model for a pinion was established based on the spatial conjugate surface theory, wherein a parabolic TE function was embedded into the tooth geometry. A numerical simulation of the tooth contact paths confirmed that the resulting transmission error curve closely followed the theoretical target. Furthermore, the contact pattern was centralized in the middle region of the tooth flank, effectively avoiding edge contact and stress concentration, thereby validating the effectiveness of the proposed flank modification.

2. The proposed digital generating machining method achieved a theoretical path deviation of less than 1.5 μm, and it has been successfully implemented on a general-purpose five-axis CNC machine. In this approach, the YW mill remained fixed during cutting, whereas the gear blank followed a precisely precomputed arc-shaped spatial motion trajectory derived from the modified flank geometry. This strategy enabled the efficient and accurate enveloping of the complex-modified tooth surface.

Three machining trials demonstrated the practical viability of the proposed method. The use of a YW mill yielded a wide cutting band, which significantly enhanced the material removal efficiency and effectively resolved the issue of dense toolpaths commonly encountered when machining spiral bevel gears with conventional ball-end mills.

Data availability

All data generated or analysed during this study are included in this published article.

References

[1] Fuentes-Aznar A , Ruiz-Orzaez R , Gonzalez-Perez I .Computational approach to design face-milled spiral bevel gear drives with favorable conditions of meshing and contact[J].Meccanica, 2018, 53(1):1-18.

[2] Zheng F, Han X, Lin H, et al. Research on the cutting dynamics for face-milling of spiral bevel gears[J]. Mechanical Systems and Signal Processing, 2021, 153: 107488.

[3] J. Wang, L. Kong, B. Liu, X. Hu, X. Yu, W. Kong, The Mathematical Model of Spiral Bevel Gears - A Review, SV-JME 60 (2014) 93 – 105. https://doi.org/10.5545/sv-jme.2013.1357.

[4] Z. Chen, M. Zeng, A. Fuentes-Aznar, Computerized design, simulation of meshing and stress analysis of pure rolling cylindrical helical gear drives with variable helix angle, Mechanism and Machine Theory 153 (2020) 103962. https://doi.org/10.1016/j.mechmachtheory.2020.103962.

[5] C. Chu, Y. Zhou, J. Zhang, J. Tang, Computational approaches for improving machining precision in five-axis flank milling of spiral bevel gears, Computers & Industrial Engineering 177 (2023) 108984. https://doi.org/10.1016/j.cie.2023.108984.

[6] Á. Álvarez, A. Calleja, N. Ortega, L. De Lacalle, Five-Axis Milling of Large Spiral Bevel Gears: Toolpath Definition, Finishing, and Shape Errors, Metals 8 (2018) 353. https://doi.org/10.3390/met8050353.

[7] G. Hlebanja, M. Erjavec, M. Hriberšek, L. Knez, S. Kulovec, Theory and Applications Based on S-Gear Geometry, in: S.P. Radzevich (Ed.), Recent Advances in Gearing, Springer International Publishing, Cham, 2022: pp. 51–87. https://doi.org/10.1007/978-3-030-64638-7_2.

[8] W. Huang, Z. Li, H. Ma, J. Zhu, Z. Liu, H. Song, H. Hu, X. Li, Y. Yang, Z. Peng, A novel analytical method for meshing characteristics of spiral bevel gears considering slice coupling, Mechanism and Machine Theory 195 (2024) 105591. https://doi.org/10.1016/j.mechmachtheory.2024.105591.

[9] Simon V V. Design and Manufacture of Spiral Bevel Gears With Reduced Transmission Errors[J].American Society of Mechanical Engineers, 2009(4).

[10] F. Li, S. Wang, P. Chen, Z. Li, L. Li, Q. Peng, Multi-objective variable parameter optimization algorithm for spiral bevel gear tooth surface considering meshing efficiency and contact performance, J Mech Sci Technol 36 (2022) 3547–3559. https://doi.org/10.1007/s12206-022-0631-7.

[11] C. Zhang, J. Wei, G. Wang, W. Gao, Investigation of dynamic stress similarity in gear transmission system considering geometric distortion: Theoretical analysis and experimental prediction, Mechanism and Machine Theory 216 (2025) 106225. https://doi.org/10.1016/j.mechmachtheory.2025.106225.

[12] G. Sciarra, G. Mottola, M. Pleguezuelos, M.B. Sánchez, M. Carricato, J.I. Pedrero, Analysis of the contact stress of beveloid gears with straight teeth and parallel axes, Mechanism and Machine Theory 214 (2025) 106156. https://doi.org/10.1016/j.mechmachtheory.2025.106156

[13] V.V. Simon, Multi-objective optimization of the manufacture of face-milled hypoid gears on numerical controlled machine tool, Proceedings of the Institution of Mechanical Engineers, Part B: Journal of Engineering Manufacture 235 (2021) 1120–1130. https://doi.org/10.1177/0954405420978039.412

[14] Zheng F, Han X, Lin H, et al. Research on the cutting dynamics for face-milling of spiral bevel gears[J]. Mechanical Systems and Signal Processing, 2021, 153: 107488.

[15] Mu Y M,Li W L,Fang Z D. Tooth surface modification methodof face-milling spiral bevel gears with high contact ratio based oncutter blade profile correction[J]. International Journal of Advanced Manufacturing Technology,2020,106(7):3229-3237.

[16] F.L. Litvin, A. Fuentes, A. Demenego, D. Vecchiato, Q. Fan, New developments in the design and generation of gear drives, Proceedings of the Institution of Mechanical Engineers, Part C: Journal of Mechanical Engineering Science 215 (2001) 747–757. https://doi.org/10.1243/0954406011524117.

[17] Y. Liu, L. Chen, X. Mao, D. Shangguan, A Semi-Analytical Loaded Contact Model and Load Tooth Contact Analysis Approach of Ease-Off Spiral Bevel Gears, Machines 12 (2024) 623. https://doi.org/10.3390/machines1209062313213

[18] P. Wang, E. Bekele Tesfa, J. Lin, Z. Shi, Generation of internal spiral bevel gears by gear skiving method, Forsch Ingenieurwes 89 (2025) 129. https://doi.org/10.1007/s10010-025-00900-4.

[19] Choudhary P, Niranjan A, Kumar P. Modeling and simulation of a bevel gear[C]//Advances in Mechanical Engineering and Technology: Proceedings of 6th International Conference on Advanced Production and Industrial Engineering (ICAPIE)-2021. Singapore: SpringerSingapore, 2022: 231-247.

[20] Das S, Abedin M M, Siddique I M. Efficient Operations through Time & Method Study: Reducing Machining Time in Bevel Gear Production[J]. European Journal of Advances in Engineering and Technology, 2024, 11(3): 81-87.

[21] R. Tan, B. Chen, C. Peng, D. Liang, D. Xiang, The geometric principles of general spiral bevel gears of local bearing contact from spatial conjugate curves, Proceedings of the Institution of Mechanical Engineers, Part C: Journal of Mechanical Engineering Science 231 (2017) 1651–1663. https://doi.org/10.1177/0954406215619649.

[22] R. Tan, B. Chen, C. Peng, X. Li, Study on spatial curve meshing and its application for logarithmic spiral bevel gears, Mechanism and Machine Theory 86 (2015) 172–190. https://doi.org/10.1016/j.mechmachtheory.2014.11.023.

[23] L. Geng, S. Nie, B. Zhao, C. Jiang, A method to remanufacture large-size spiral bevel gear with ease-off topology modification by face-milled generator, Advances in Mechanical Engineering 15 (2023) 16878132231194322. https://doi.org/10.1177/16878132231194322.

[24] W. Zhang, R. Tan, X. Guo, B. Chen, R. Shu, F. Zheng, Analytical synthesis of the kinematic geometry of spiral bevel gears of pure-rolling contact, Mechanism and Machine Theory 153 (2020) 103992. https://doi.org/10.1016/j.mechmachtheory.2020.103992.

[25] Z. Chen, H. Zhang, X. Xiao, C. He, K. Zhu, Y. Chen, A. Fuentes-Aznar, Computerized design of asymmetric pure rolling gears with a method for predesigning the desired function of unloaded transmission errors, Mechanism and Machine Theory 213 (2025) 106072. https://doi.org/10.1016/j.mechmachtheory.2025.106072.

[26] ISO. 1328-1:2013, Cylindrical gears — ISO system of flank tolerance classification —Part 1:Definitions and allowable values of deviations relevant to flanks of gear teeth[S]. Geneva: International Organization for Standardization, 2013.

Acknowledgments

We would like to thank Editage (http://www.editage.cn) for English language editing.

Funding

We would like to thank the financial aid and support from the National Natural Science Foundation of China(No.52275052), and Natural Science Foundation of Chongqing (No.CSTB2022NSCQ-MSX0475). The authors of the paper express their deep gratitude to them for the financial support of research projects.

Author contributions

The idea for the paper came from R.T. and W.W.R.T. and W.Z. acquired the funding and

administered the project; Y.L. developed the methodology and conducted the formal analysis and validation; W.W. and F.X. were responsible for the investigation and visualization; R.T., Y.L. and W.W. wrote the paper.

competing interests

The authors declare no competing interests.

Appendix: Coordinate transformation matrixes

$$\boldsymbol{M}_{01}=\begin{pmatrix}\cos(\phi) & -\sin(\phi) & 0 & 0\\ \sin(\phi) & \cos(\phi) & 0 & 0\\ 0 & 0 & 1 & 0\\ 0 & 0 & 0 & 1\end{pmatrix}. \tag{43}$$

$$\boldsymbol{M}_{p0}=\begin{pmatrix}1 & 0 & 0 & 0\\ 0 & \cos(\xi) & -\sin(\xi) & 0\\ 0 & \sin(\xi) & \cos(\xi) & 0\\ 0 & 0 & 0 & 1\end{pmatrix}. \tag{44}$$

$$\boldsymbol{M}_{2p}=\begin{pmatrix}\cos(\phi) & -\sin(\phi) & 0 & 0\\ \sin(\phi) & \cos(\phi) & 0 & 0\\ 0 & 0 & 1 & 0\\ 0 & 0 & 0 & 1\end{pmatrix}=\begin{pmatrix}\cos(i_{21}\varphi) & -\sin(i_{21}\varphi) & 0 & 0\\ \sin(i_{21}\varphi) & \cos(i_{21}\varphi) & 0 & 0\\ 0 & 0 & 1 & 0\\ 0 & 0 & 0 & 1\end{pmatrix}. \tag{45}$$

$$\boldsymbol{M}_{21}=\begin{pmatrix}\cos(\varphi)\cos(\phi)+\sin(\phi)\sin(\varphi)\cos(\xi) & \cos(\phi)\cos(\xi)\sin(\varphi)-\cos(\varphi)\sin(\phi) & \sin(\varphi)\sin(\xi) & 0\\ \cos(\varphi)\cos(\xi)\sin(\phi)-\cos(\phi)\sin(\varphi) & \cos(\varphi)\cos(\xi)\cos(\phi)+\sin(\varphi)\sin(\phi) & \cos(\phi)\sin(\xi) & 0\\ -\sin(\phi)\sin(\xi) & -\cos(\phi)\sin(\xi) & \cos(\xi) & 0\\ 0 & 0 & 0 & 1\end{pmatrix}. \tag{46}$$

$$\boldsymbol{M}_{10}=\boldsymbol{M}_{01}{}^{T}. \tag{47}$$

$$\boldsymbol{M}_{21}=\boldsymbol{M}_{2p}\boldsymbol{M}_{p0}\boldsymbol{M}_{01}. \tag{48}$$

Additional information

Correspondence and requests for materials should be addressed to Y.L.

Reprints and permissions information is available at www.nature.com/reprints.

Publisher's note Springer Nature remains neutral with regard to jurisdictional claims in publish ed maps and institutional affiliations.